AGU PUBLICATIONS

JGR

Journal of Geophysical Research: Oceans

RESEARCH ARTICLE

10.1002/2016JC012190

# Interannual and interdecadal variability of the North Equatorial Countercurrent in the Western Pacific

**Xiao Chen[1,2,3], Bo Qiu[3], Yan Du[1], Shuiming Chen[3], and Yiquan Qi[1,4]**

[1]State Key Laboratory of Tropical Oceanography, South China Sea Institute of Oceanology, Chinese Academy of Sciences, Guangzhou, China, [2]University of Chinese Academy of Sciences, Beijing, China, [3]Department of Oceanography, University of Hawaii at Manoa, Honolulu, Hawaii, USA, [4]College of Oceanography, Hohai University, Nanjing, China

**Key Points:**
- Interannual NECC variability develops prior to mature phase of ENSO
- Coherent intensity, position, and width changes of NECC on interdecadal timescale
- Similar interdecadal changes in tropical trade wind system

**Correspondence to:**
B. Qiu,
bo@soest.hawaii.edu

**Citation:**
Chen, X., B. Qiu, Y. Du, S. Chen, and Y. Qi (2016), Interannual and interdecadal variability of the North Equatorial Countercurrent in the Western Pacific, *J. Geophys. Res. Oceans*, *121*, 7743–7758, doi:10.1002/2016JC012190.

Received 28 JUL 2016
Accepted 4 OCT 2016
Accepted article online 6 OCT 2016
Published online 21 OCT 2016

**Abstract** Interannual and longer timescale variations of the North Equatorial Countercurrent (NECC) in the western Pacific are investigated using the multidecade (1960–2014) hindcast by the Ocean general circulation model for the Earth Simulator (OFES). The OFES-simulated sea level and upper ocean circulation changes show favorable comparisons with available tide gauge data and repeat hydrographic surveys along the 137°E meridian. An empirical orthogonal function (EOF) analysis reveals that the low-frequency NECC variability is dominated by two distinct modes. The first mode fluctuates interannually and shows strengthening and southward migration of the NECC concurrent with the development of El Niño events. Unlike the extratropical western Pacific Ocean circulation variability controlled by wind forcing west of the dateline, the interannual NECC variations are forced by equatorial wind forcing cumulative across the entire Pacific basin. The second mode of the NECC variability has an interdecadal timescale and is characterized by NECC's progressive weakening in strength, migrating poleward, and broadening in width over the past 50 years. These long-term changes in NECC are caused by the corresponding changes in the trade wind system that weakened and expanded poleward in the past half a century across the Pacific basin.

## 1. Introduction

In the low-latitude northwestern Pacific Ocean, the upper ocean zonal circulation is dominated by the wind-driven westward-flowing North Equatorial Current (NEC) and eastward-flowing North Equatorial Countercurrent (NECC). By transporting water masses from the interior subtropical and tropical gyres into the western boundary, the time-varying NEC controls the material and heat exchanges and partitioning between the tropical and subtropical North Pacific (see *Hu et al*. [2015] and *Qiu et al*. [2015] for comprehensive reviews on the NEC). The NECC, on the other hand, serves as a confluent "return flow" for the low-latitude western boundary currents: the Mindanao Current (MC) off the Philippine coast and the New Guinea Coastal Current (NGCC) off the New Guinea coast [*Lukas et al*., 1991; *Gordon and Fine*, 1996; *Kashino et al*., 2001; *Tozuka et al*., 2002; *Hsin and Qiu*, 2012a; *Chen et al*., 2015]. Located across the latitudinal center of the western Pacific warm pool, the NECC has been observed and modeled to play important roles in the maintenance and heat budget variability of the warm pool [*Meyers and Donguy*, 1984; *Picaut and Delcroix*, 1995; *Clement et al*., 2005].

By accumulating perturbations from the ocean interior either via low-mode baroclinic Rossby waves or in the form of isolated mesoscale eddies, both the NEC and NECC in the tropical northwestern Pacific have been observed to be highly variable in space and time. Compared to the NEC that exists in the 9°N–18°N band of the western Pacific basin, detecting the NECC variability in its 1°N–8°N band has been observationally more challenging due to the smaller Coriolis parameter. In addition, mismatch in potential vorticity between the MC outflow and the interior Sverdrup circulation renders the NECC a dynamically highly unstable current system [e.g., *Qiu and Lukas*, 1996; *Chen et al*., 2015]. Due to these constraints, studies of the NECC variability based on expendable bathythermograph (XBT) and repeat hydrographic surveys have been often fragmentary and subject to large measurement uncertainties [*Delcroix et al*., 1987; *Qiu and Joyce*, 1992; *Gouriou and Toole*, 1993; *Reverdin et al*., 1994; *Donguy and Meyers*, 1996; *Johnson et al*., 2002].

The advent of satellite altimetry in the 1990s has improved the spatial and temporal detection of the time-varying NECC and many recent investigations have utilized the altimeter-derived sea surface height (SSH) data to explore the seasonal-to-interannual variations of the NECC [*Bonjean and Lagerloef*, 2002; *Heron et al*.,

2006; *Hsin and Qiu*, 2012a,2012b; *Zhao et al*., 2013; *Chen et al*., 2015]. In our preceding investigation [*Chen et al*., 2015], we focused on the seasonal eddy kinetic energy (EKE) modulations along the NECC path, with the aid of an eddy-resolving ocean general circulation model (OGCM), and identified barotropic instability of the laterally sheared NECC to be the cause for the observed EKE modulations.

In this paper, we expand this previous study of ours and examine the NECC variability on the timescales from interannual to interdecadal. By using the output from the global eddy-resolving OGCM for the Earth Simulator (OFES) that covers the period from 1960 to 2014, we first verify the modeled SSH and velocity variations associated with the NECC against the long-term tide gauge measurements and repeat hydrographic surveys. Following verification, we extract the dominant modes of the NECC variability through an empirical orthogonal function (EOF) analysis. To better understand the modes of the NECC variability with different timescales, we adopt a $1^1/_2$-layer reduced-gravity model and quantify the effects of surface wind forcing over the past half century.

## 2. Data

Output of the eddy-resolving OGCM for the Earth Simulator (OFES) [*Masumoto et al*., 2004; *Sasaki et al*., 2008] is used in this study. Based on the Modular Ocean Model (MOM3) [*Pacanowski and Griffies*, 2000], the quasiglobal OFES model extends from 75°S to 75°N and has a 0.1° × 0.1° horizontal resolution and 54 vertical levels. Initialized from a state of rest with the World Ocean Atlas 1998 (WOA98) [*Boyer and Levitus*, 1997], the model is spun up for 50 years with the climatological forcing data of the National Centers for Environmental Prediction/National Center for Atmospheric Research (NCEP-NCAR) reanalysis [*Kalnay et al*., 1996]. After the 50 year spin-up integration, a hindcast simulation from 1950 to 2014 is conducted with the daily atmospheric forcing from the NCEP-NCAR reanalysis. For this study, the monthly output of the OFES hindcast simulation will be used to avoid model's transition from its climatological to hindcast integration, we will focus the analysis period from 1960 to 2014.

In order to check the validity of the multidecade OFES simulation output in the tropical northwestern Pacific of our interest, we utilize two in situ observational data sources for comparison. The first data source is the long-term sea level records available from the Sea Level Center of University of Hawaii (http://uhslc.soest.hawaii.edu/data/). With our interest in the NECC's variability, three tide gauge stations straddling the NECC are selected: Malakal, Yap, and Kapingamarangi. Locations of these tide gauge stations are marked with green stars in Figure 1a. The second data source is the repeat hydrographic surveys along the 137°E meridian from 3°N to 34°N by Japan Meteorological Agency (JMA). Initiated in winter of 1967, repeat temperature/salinity measurements have been maintained by JMA on various frequencies per year [see *Nakano et al*., 2005; *Qiu and Joyce*, 1992]. Within the period of 1967–2014, a total of 131 surveys have been conducted and the temperature/salinity data from these cruises are used in this study. Unlike the tide gauges sea level records, repeat hydrographic data allow us to quantify the veracity of the interannual and longer timescale variability of the OFES simulation throughout the upper ocean water column.

## 3. Verification of OFES Simulation

OFES simulates well the time-mean circulation features in the western tropical Pacific at both surface (0–150 m) and subsurface (150–300 m) layers. As shown in Figure 1a, the eastward-flowing NECC is found to exist in the 2°N–8°N band of the surface 150 m layer. Below the 150 m depth (Figure 1b), the NECC disappears; instead an eastward subsurface jet that has its origin in both the southward-flowing MC along the Philippine coast and the northwestward-flowing New Guinea Coastal Undercurrent (NGCUC) along the New Guinea coast, appears and flows roughly along 2°N (see also Figure 2a). East of 140°E, the eastward subsurface jet transforms into the Equatorial Undercurrent (EUC) in this 150–300 m subsurface layer. In the 0–150 m surface layer, the NECC is sandwiched by the westward-flowing NEC to the north and the westward-flowing South Equatorial Current (SEC) to the south. Within the zonal band of 5°S–8°S, Figure 1a reveals that the eastward-flowing South Equatorial Countercurrent (SECC) exists to the east of 155°E. Compared to its northern hemisphere countercurrent, the SECC is weaker, but is similarly confined to the surface 150 m layer.

Notice that the confinement of the NECC in the surface 150 m layer is seen in the geostrophic zonal velocity pattern calculated from the JMA repeat hydrographic surveys (Figure 2b). Aside from the NECC, westward flows of the NEC and that beneath of the NEC, and the thermal structures, such as the thermal ridge

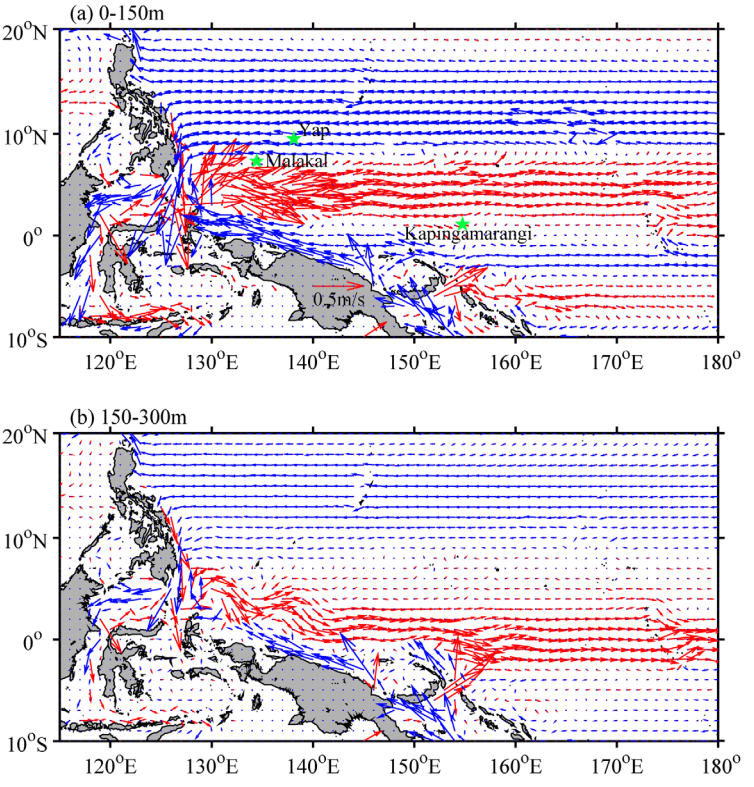


**Figure 1.** Long-term mean velocity field in the western Pacific averaged in (a) 0–150 m layer and (b) 150–300 m layer from the OFES simulation of 1960–2014. Velocity vectors with an eastward (westward) component are plotted in red (blue). Velocity scale is indicated in Figure 1a near 5°S and 140°E. Green stars in Figure 1a denote the tide gauge locations of Malakal (7.328°N, 134.45°E), Yap (9.514°N, 138.125°E), and Kapingamarangi (1.1°N, 154.783°E).

centered at 8°N in the upper ocean and the subsurface thermal doming centered at 7°N, all compare favorably between the OFES simulation climatology and the long-term JMA observations.

In terms of the simulated time-varying signals, we compare in Figure 3 the monthly time series of sea level anomalies from the OFES (blue lines) and the tide gauge stations at Malakal, Yap, and Kapingamarangi (red lines). There exists an overall good correspondence between the modeled and observed sea level fluctuations, and the OFES simulation is able to capture most of the seasonal and interannual sea level peaks in the observations. The linear correlation coefficients between the modeled and observed time series at Malakal, Yap, and Kapingamarangi are 0.53, 0.51, and 0.82, respectively.

## 4. Analysis of OFES Output

An objective way to identify the dominant modes of the ocean circulation variability is through the EOF analysis. With the region of our interest encompassing the equator (10°S–20°N, 115°E–180°E), we choose to use the velocity data averaged in the upper 150 m layer in order to better capture the overall fluctuations

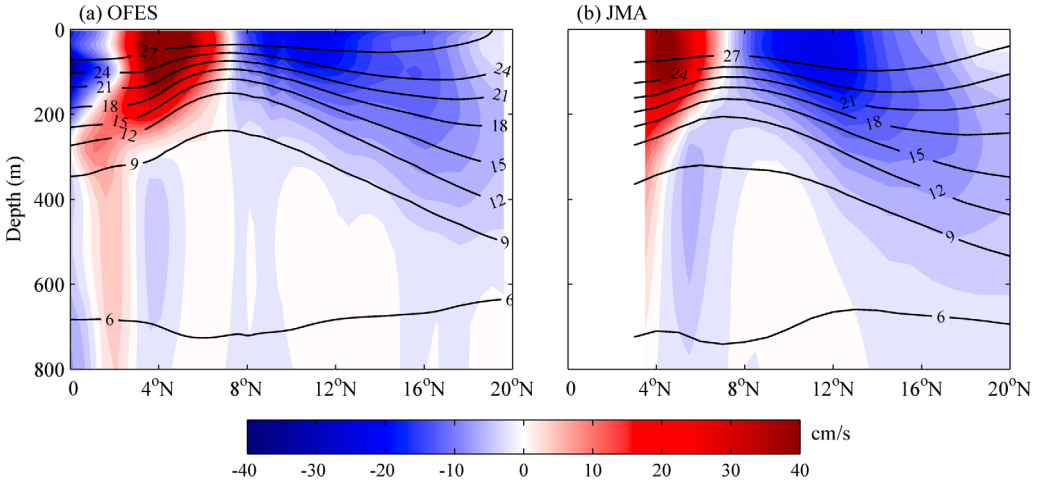


**Figure 2.** Long-term mean zonal velocity distribution along 137°E from (a) the OFES simulation of 1967–2014 and (b) the JMA repeat hydrographic surveys of 1967–2014. The reference level for geostrophic flow calculation in Figure 2b is chosen as 1000 dbar.

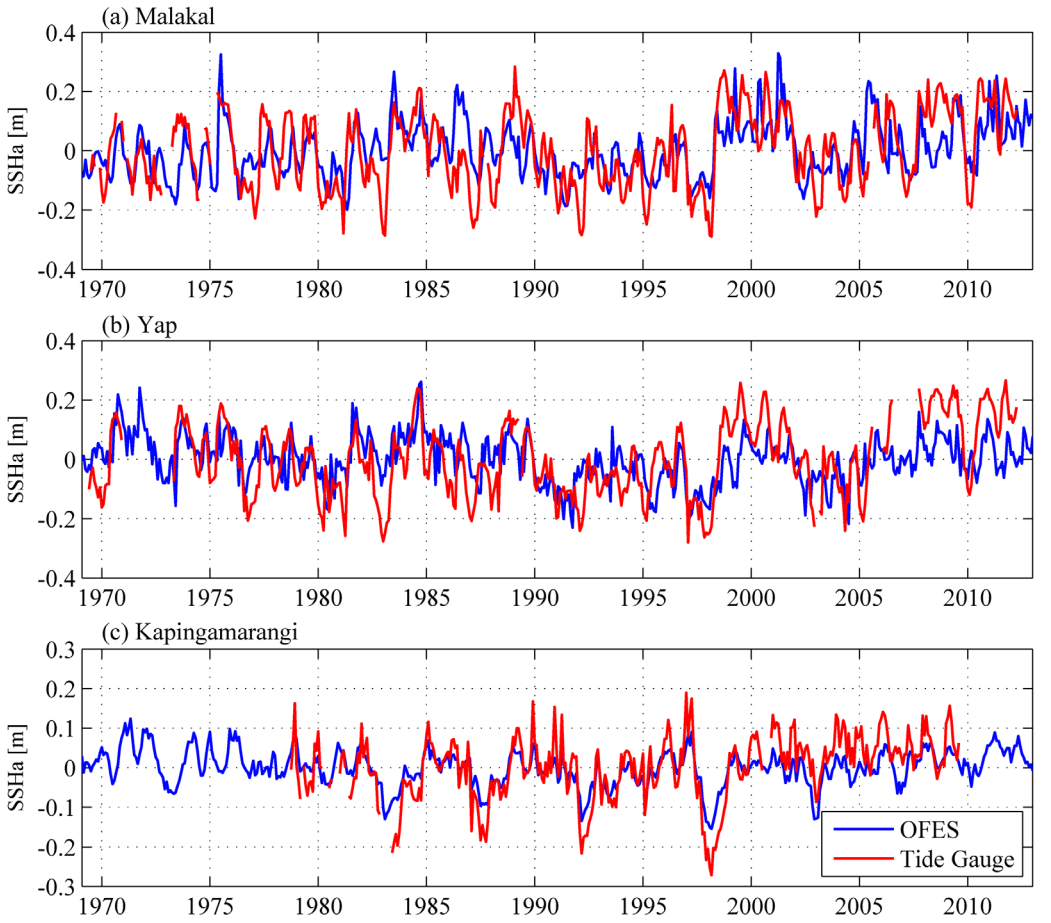


**Figure 3.** Comparison of SSH anomalies between tide gauge measurements (red lines) and the OFES simulation (blue lines) at (a) Malakal, (b) Yap, and (c) Kapingamarangi. The correlation coefficients at (a), (b), and (c) are 0.53, 0.51, and 0.82, respectively. The tide gauge locations are shown with green stars in Figure 1a.

of the NECC. As the seasonal fluctuations of the NECC in the western tropical Pacific Ocean were the focus of our preceding investigations [*Chen et al.*, 2015], we apply a 13 month running-mean filter to the original monthly $u/v$ field of the OFES output before the EOF analysis to limit the scope of this study to the NECC changes on the interannual and longer timescales.

### 4.1. Mode of Interannual Variability

The EOF analysis reveals two dominant modes in the region of our selection. Mode-1 accounts for 34% of the variance and its spatial pattern and principal component are shown in Figures 4a and 4b, respectively. This leading mode is dominated by interannual fluctuations and its center of action is located along the equatorial band of 8°S–8°N. When the principal component of mode-1 (PC1) is positive, Figure 4a reveals that the eastward-flowing NECC, which exists nominally in the 1°N–8°N band (recall Figure 1a), intensifies on its southern half but weakens on its northern half. Dynamically, this spatial pattern implies an equatorward swift by both the NECC and NEC when PC1 is in its positive phase.

Given the spatial confinement of this mode to the equatorial band and its interannual temporal variability, it is natural to seek its connection to the modulation of El Niño/Southern Oscillation (ENSO) variability. Figure 5a compares the time series of Niño-3.4 index with that of PC1. Defined by SST anomalies averaged in the region 5°S–5°N and 170°W–120°W, the Niño-3.4 index is a commonly used index to represent the time-varying ENSO state. A favorable correspondence between the two time series is easily discernible and this is particularly true after 1970. The lead-lag correlation analysis (Figure 5b) indicates that PC1 is skewed to have a lead of 1–2 months ahead of the Niño-3.4 index, suggesting that the variability of mode-1 identified in this study in the western tropical Pacific Ocean occurs during the developing phase of ENSO event.

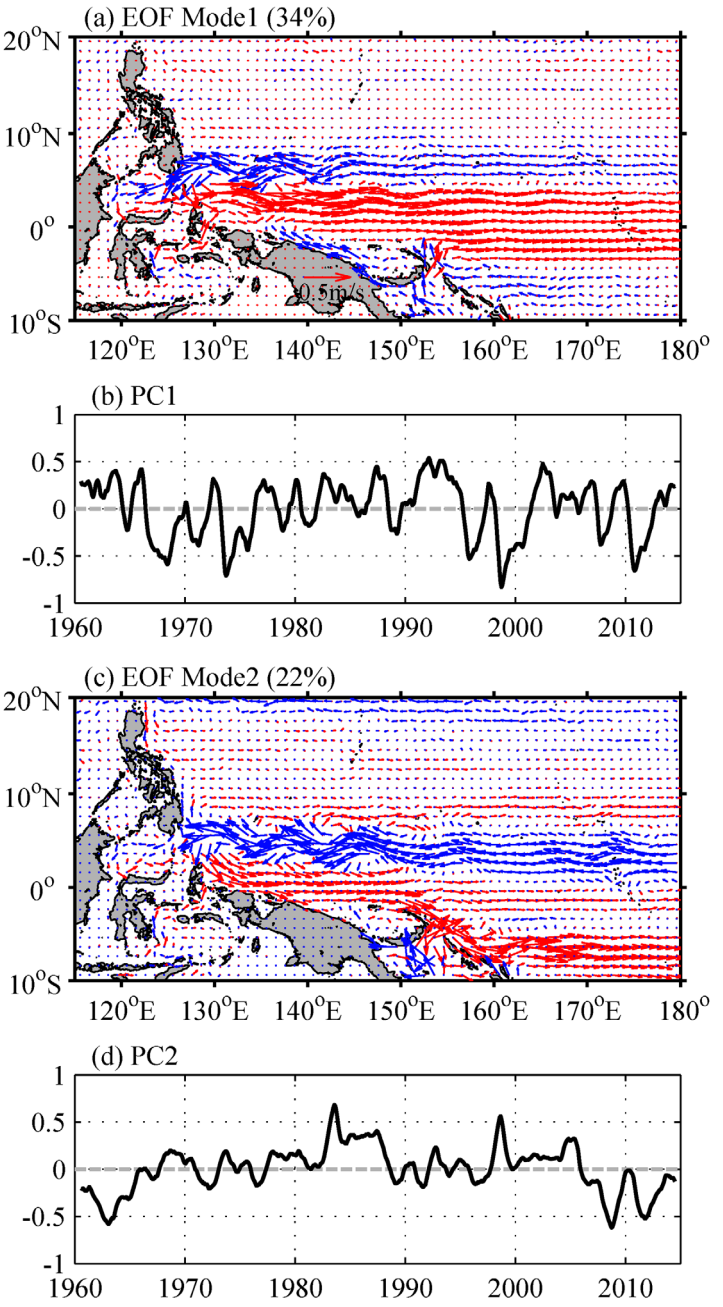


**Figure 4.** (a, b) Spatial pattern and principal component of EOF mode-1 of the 0–150 m layer velocity field from the OFES simulation. (c, d) Same as Figures 4a and 4b except for the EOF mode-2.

In order to examine the vertical structures associated with the mode-1 variability, we plot in Figure 6b the zonal-mean *u* velocity from 135°E to 155°E regressed to PC1. Compared to the climatological zonal-mean *u* velocity pattern shown in Figure 6a, the regressed result confirms that much of the mode-1 variability is confined to the surface 150 m layer and that when PC1 $>0$ (during El Niño years), both the NECC and NEC strengthen and migrate equatorward. Also clear from Figure 6b is that the eastward-flowing EUC in the subsurface layer of 150–300 m reduces in magnitude when PC1 is positive. As will become clear in section 5.1, the weakening of the EUC is due to the drop in zonal pressure gradient associated with the reduced equatorial trade winds during the El Niño events.

To evaluate robustness of the EOF mode-1 and its vertical structures shown in Figure 6b from the OFES simulation, we conducted a parallel EOF analysis on the zonal geostrophic velocity derived from the JMA repeat hydrographic surveys along 137°E. As winter is the only season in which the repeat surveys have been carried out uninterruptedly throughout the period of 1967–2014, only the winter cruise data are used in this parallel EOF analysis. Figures 7b and 7c (red line) show the spatial pattern and principal component of mode-1 based on the JMA-derived zonal velocity field. The mode-1 explains 48% of the observed zonal velocity variance. For comparison, we show in Figures 7a and 7c (blue line) the same EOF mode-1 result based on the OFES's January zonal velocity field. Despite being based on the synoptic surveys, the JMA EOF result detects a vertical structure very similar to that captured in the winter-time OFES simulation. Temporally, the observed and modeled PC1s reveal very similar time-varying fluctuations and the linear correlation coefficient between the two time series in Figure 7c reaches 0.65. It is worth emphasizing that the EOF mode-1 results shown in Figure 7 based on the winter-time OFES and JMA data show a favorable correspondence to the EOF mode-1 results on the full OFES output. For example, the correlation between the OFES PC1 shown in Figures 4b and 7c is as high as 0.83 and when PC1 is positive, both Figures 6b and 7a indicate the equatorward migration of NECC and NEC. Dynamically, this good correspondence emerges because the El Niño events reach

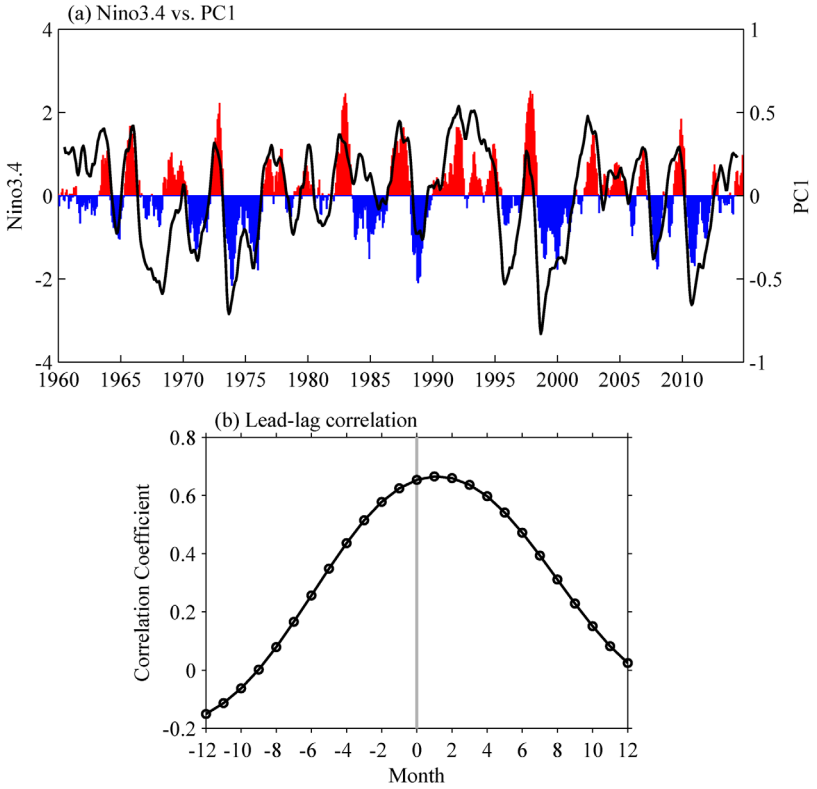


**Figure 5.** (a) Time series of the Niño-3.4 index (color bars) versus EOF PC1 (black line); (b) lead-lag correlation between Niño-3.4 index and PC1. Positive values in *x* axis indicate lead by the EOF PC1.

their mature phase in winter [e.g., *Philander*, 1990] and, as such, the winter JMA and OFES data are able to capture the dominant ENSO signals as represented by the EOF mode-1 from the full OFES simulation.

### 4.2. Mode of Interdecadal Variability

EOF mode-2 of the OFES simulation accounts for 22% of the upper ocean (0–150 m) velocity variance. As shown in Figure 4d, decadal and longer timescale fluctuations dominate the PC of this mode. In terms of its spatial pattern, the action center of this mode is again gravitated toward along the path of NECC (Figure 4c). Starting from 1960 to mid-1980s, the EOF mode-2 indicates that the eastward-flowing NECC weakened steadily, and so did the NEC, the SEC, and the NGCC. This weakening trend in the first half of our analysis period seems to be halted, or even reversed, after mid-1980s. Vertically, the EOF mode-2 signals appear to have a somewhat deeper expression than that of mode-1 (see Figure 6c).

To examine in more detail the interdecadal variability of the NECC relating to PC2, we evaluate the NECC's transport, axis position, and axis width changes defined by

$$T(x,t)=\int_{0^\circ}^{10^\circ N}\bar{u}(x,y,t)dy, \tag{1}$$

$$Y(x,t)=\frac{\int_{0^\circ}^{10^\circ N}\bar{u}(x,y,t)\cdot ydy}{\int_{0^\circ}^{10^\circ N}\bar{u}(x,y,t)dy}, \tag{2}$$

$$W(x,t)=\frac{\int_{0^\circ}^{10^\circ N}\bar{u}(x,y,t)|y-Y|dy}{\int_{0^\circ}^{10^\circ N}\bar{u}(x,y,t)dy}. \tag{3}$$

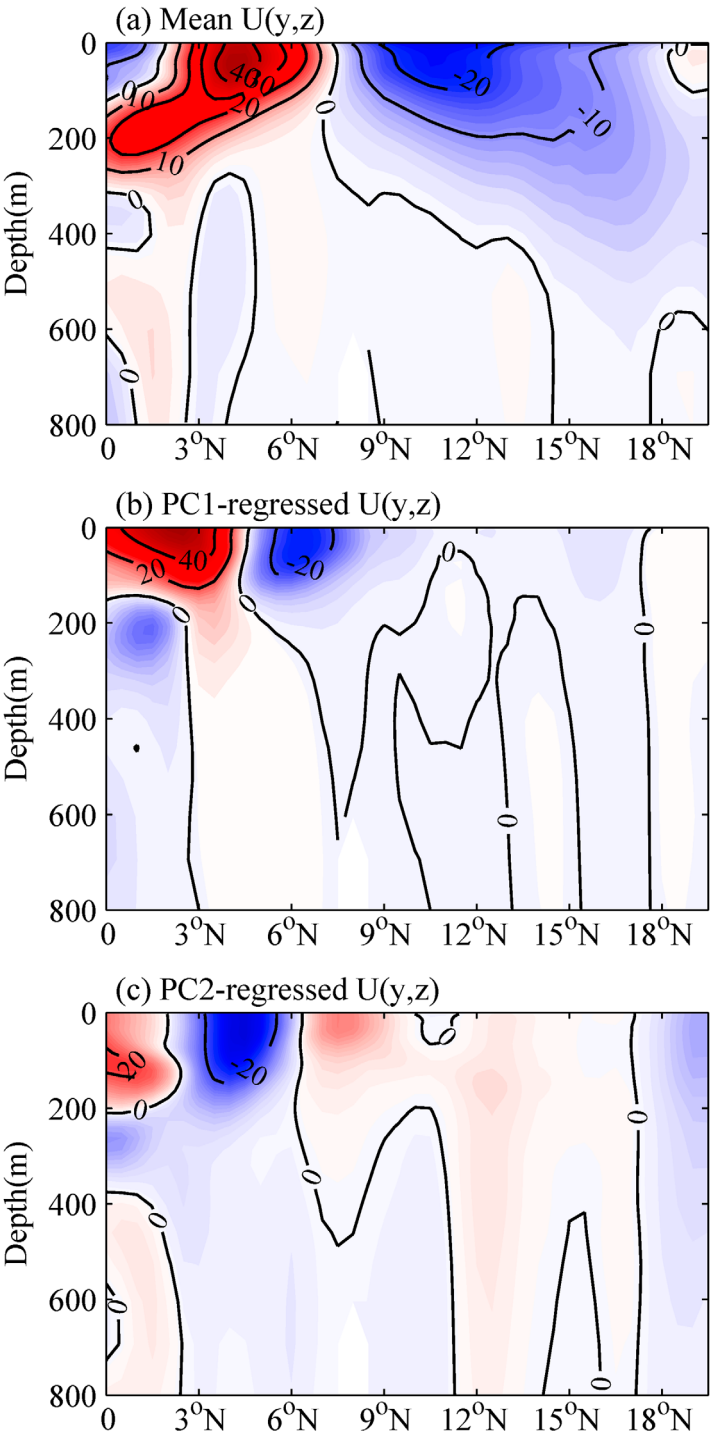


**Figure 6.** (a) Long-term zonal velocity profile averaged from 135°E to 155°E from the OFES simulation of 1960–2014. (b) Zonal velocity profile from 135°E to 155°E regressed to PC1 shown in Figure 4b. (c) Same as Figure 6b except for regressed to PC2 shown in Figure 4d. Notice that Figures 6b and 6c show the anomalous zonal flows related to the PCs. The total zonal flow is the sum of the mean U(y,z) shown in Figure 6a plus the PC-regressed U(y,z) multiplied by the PC coefficient.

In equations (1–3), $\bar{u}(x,y,t)$ is the zonal velocity integrated in the upper 0–150 m layer and is set to be zero if it is westward. Dynamically, a larger $W(x,t)$ signifies a laterally broader and more diffused NECC, and a smaller $W(x,t)$ means a narrower and better-defined NECC jet. Figure 8 shows the time series of $T(t)$, $Y(t)$, and $W(t)$ after averaging zonally from $x=$ 135°E to 155°E and applying a 13 month running-mean filter. Consistent with the EOF mode-2 result, the zonal-mean NECC transport has a decreasing trend from 1960 to mid-1980s (Figure 8a). Thereafter, the transport change leveled off; instead, the zonal-mean axis position of NECC shifted northward (Figure 8b) and its axis width increased spatially (Figure 8c). It is important to emphasize that the EOF mode-2 is only able to capture the spatially stationary part of the interdecadal NECC variations. The long-term, nonstationary changes in the NECC's axis location and width as depicted in Figures 8b and 8c are not properly represented by the EOF analysis.

## 5. NECC's Variability Versus Wind Forcing

It has been well established by previous studies that the upper ocean circulation variability in the tropical Pacific is induced by surface wind forcing and that such variability can be quantitatively investigated by a $1^1/_2$-layer reduced-gravity model [e.g., *Meyer*, 1979; *Kessler*, 1990; *Qiu and Chen*, 2010; *Capotondi and Alexander*, 2001; *Capotondi et al.*, 2003; *Zhao et al.*, 2013]. In order to better understand the forcing responsible for the NECC changes identified in the preceding section, we adopt in this section the $1^1/_2$-layer reduced-gravity model and explore, respectively, the interannual and multidecadal variations of the NECC.

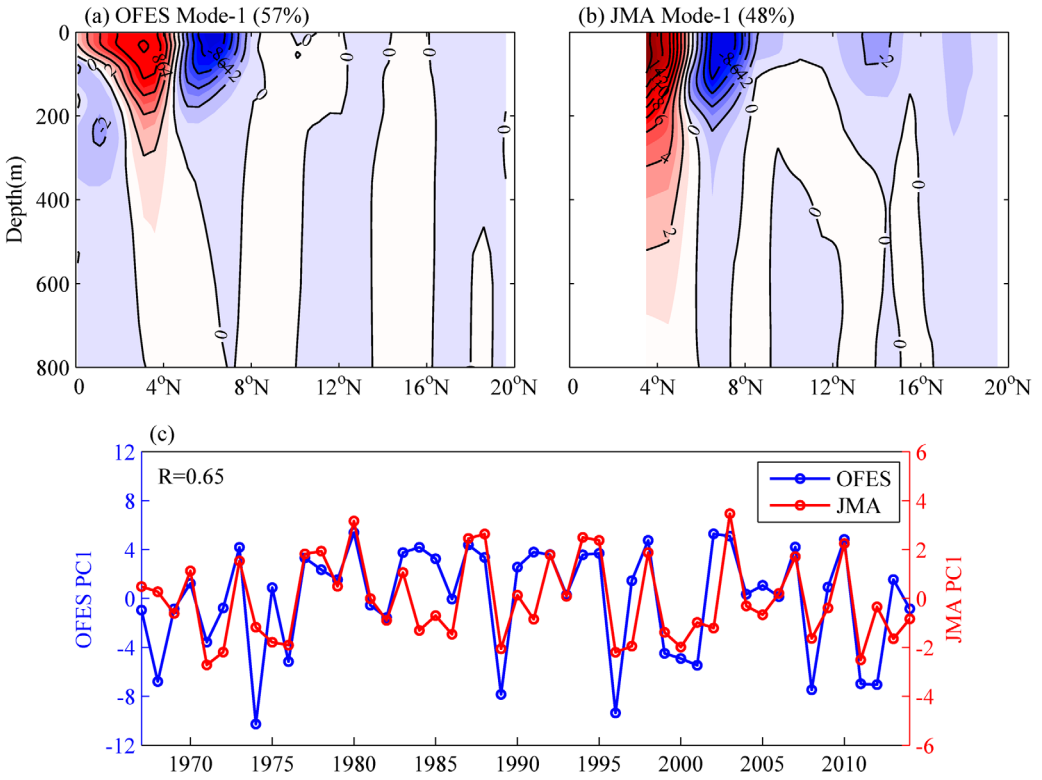


**Figure 7.** (a) Spatial pattern of EOF mode-1 of the January zonal velocity field along 137°E from the OFES simulation of 1976–2014. (b) Same as Figure 7a except from the January repeat hydrographic surveys by JMA from 1967 to 2014. (c) Principal component of the OFES mode-1 (blue line) versus the JMA mode-1 (red line) shown in Figures 7a and 7b, respectively.

### 5.1. Interannual NECC Variability

To relate the NECC's interannual variations to the tropical wind forcing, it is useful to extract the SSH signals related to the EOF mode-1 presented in Figures 4a and 4b. To do so, we regress the OFES monthly SSH field against the PC1 time series and the resultant, PC1-regressed, SSH distribution in the region of 10°S–10°N and 115°E–180° is shown in Figure 9a. From geostrophy, the prominent SSH trough residing along 5°N in Figure 9a corresponds to the anomalous westward (eastward) zonal flow along the 5°N–9°N (1°N–5°N) band shown in Figure 4a. Due to the dominance of the SSH trough along 5°N, it is not surprising to find that the PC1 time series (blue line in Figure 9b) is well represented by the SSH signals averaged in the 2.5°N–7.5°N and 130°E–165°E box (red line in Figure 9b). The two time series in Figure 9b have a linear correlation coefficient reaching 0.77. Physically, this high correlation implies that examining the interannual NECC variability becomes equivalent to examining the time-varying SSH anomaly signals in the 2.5°N–7.5°N and 130°E–165°E box along the climatological NECC path (i.e., the white dashed box in Figure 9a).

Under the long-wave approximation, the linear vorticity equation governing the SSH anomaly $h'(x,y,t)$ in the $1^1/_2$-layer reduced-gravity model is given by

$$\frac{\partial h'}{\partial t} - C_R \frac{\partial h'}{\partial x} = -\frac{g'}{g\rho_0} \nabla \times \left( \frac{\vec{\tau}}{f} \right) - \varepsilon h', \tag{4}$$

where $C_R(x,y)$ is the phase speed of long baroclinic Rossby waves, $g'$ is the reduced gravity, $\rho_0$ is the reference density, $\vec{\tau}$ is the surface wind stress anomaly vector, and $\varepsilon$ is the Newtonian dissipation rate. Integrating equation (4) from the eastern boundary ($x=x_e$) along the characteristic of baroclinic Rossby waves (constant $y$ in the present case), $h'(x,y,t)$ can be solved by

$$h'(x,y,t) = \frac{g'}{g\rho_0} \int_{x_e}^{x} \frac{1}{C_R} \nabla \times \left[ \vec{\tau}(x', y, t + \frac{x - x'}{C_R})/f \right] \times \exp\left[ \frac{\varepsilon}{C_R}(x - x') \right] dx'. \tag{5}$$

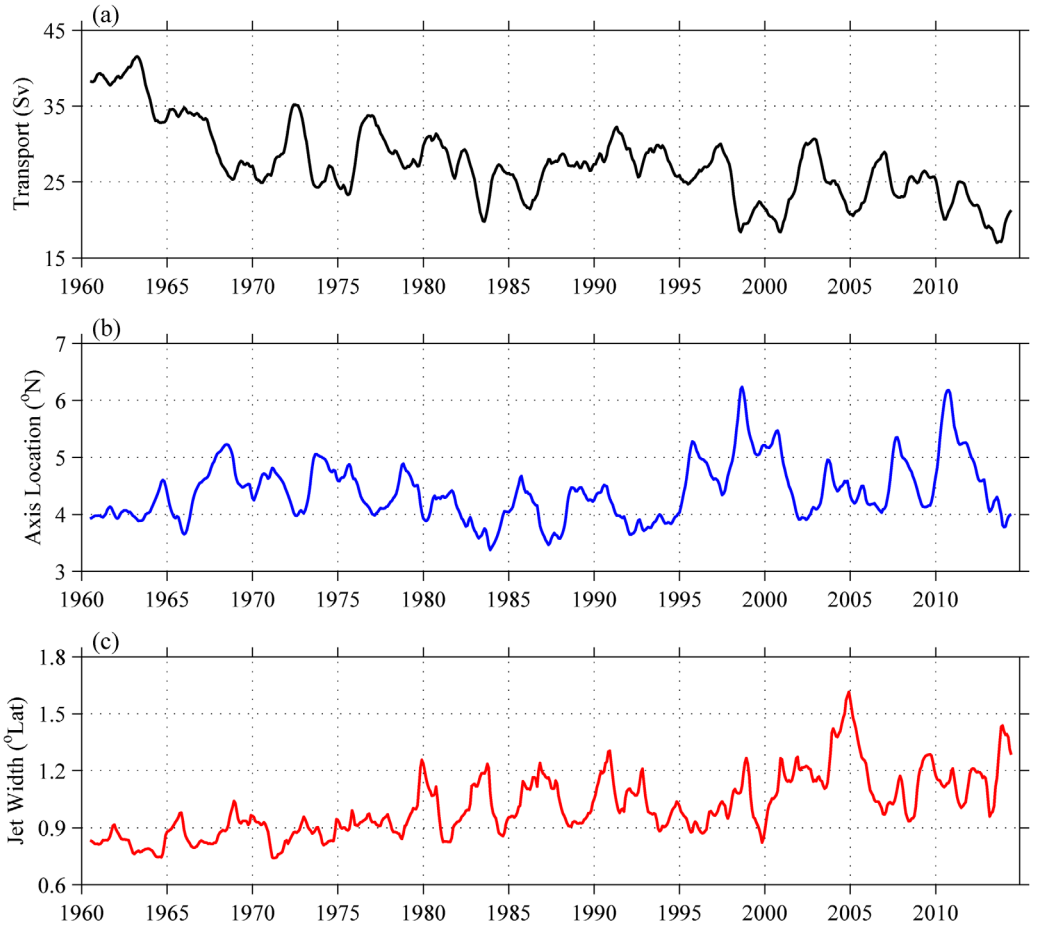


**Figure 8.** Time series of (a) NECC's transport, (b) axis location, and (c) jet width averaged in the zonal section of 135°E–155°E. See equations (1)–(3) for definitions. A 13 month running-mean filter has been applied to the time series.

In equation (5), we have ignored the signal of SSH anomalies at the eastern boundary as its effect has been shown to have little impact on the SSH variability in the western Pacific [*Fu and Qiu*, 2002]. For the parameters $g'$ and $\varepsilon$, their values ($g'=0.05$ m/s$^2$ and $\varepsilon^{-1}=1.6$ year) are determined by matching the modeled and observed rms amplitudes of the $h'$ time series at the western Pacific tide gauge stations (recall Figure 3). Figure 9c (blue line) shows the SSH anomaly time series in the box of 2.5°N–7.5°N and 130°E–165°E evaluated from equation (5) with the use of monthly wind stress data from the NCEP-NCAR reanalysis. With their linear correlation coefficient at 0.89, the ability of the simple 1½-layer reduced-gravity model in capturing the OFES-derived low-frequency SSH changes (red line in Figure 9c) can be easily confirmed.

One merit of adopting the linear vorticity equation (4) is it provides us with a means to quantify the relative contributions of wind forcing in different parts of the Pacific basin that is responsible for the interannual NECC changes. To pursue this, it is helpful to define

$$\bar{h}'(X,t)=\frac{g'}{\rho_o g L_x L_y}\int_{2.5^\circ\mathrm{N}}^{7.5^\circ\mathrm{N}}\int_{130^\circ\mathrm{E}}^{165^\circ\mathrm{E}}\left\{\int_X^x \frac{1}{C_R}\nabla\times\left[\vec{\tau}\left(x',y,t+\frac{x-x'}{C_R}\right)\Big/ f\right]\exp\frac{\varepsilon(x-x')}{C_R}dx'\right\}dxdy, \tag{6}$$

where $L_xL_y$ denotes the area of the NECC box of our interest (i.e., 2.5°N–7.5°N and 130°E–165°E). Physically, $\bar{h}'(X,t)$ indicates the SSH anomalies averaged in the NECC box induced by the wind forcing that exists west of longitude $X$. By definition, $\bar{h}'(x_e,t)$ gives the time series forced by the basin-wide wind forcing and is shown by the blue line in Figure 9c.

In Figure 10a, we plot the variance of the $\bar{h}'(x_e,t)$ time series explained by the wind forcing west of $X$ as a function of longitude:

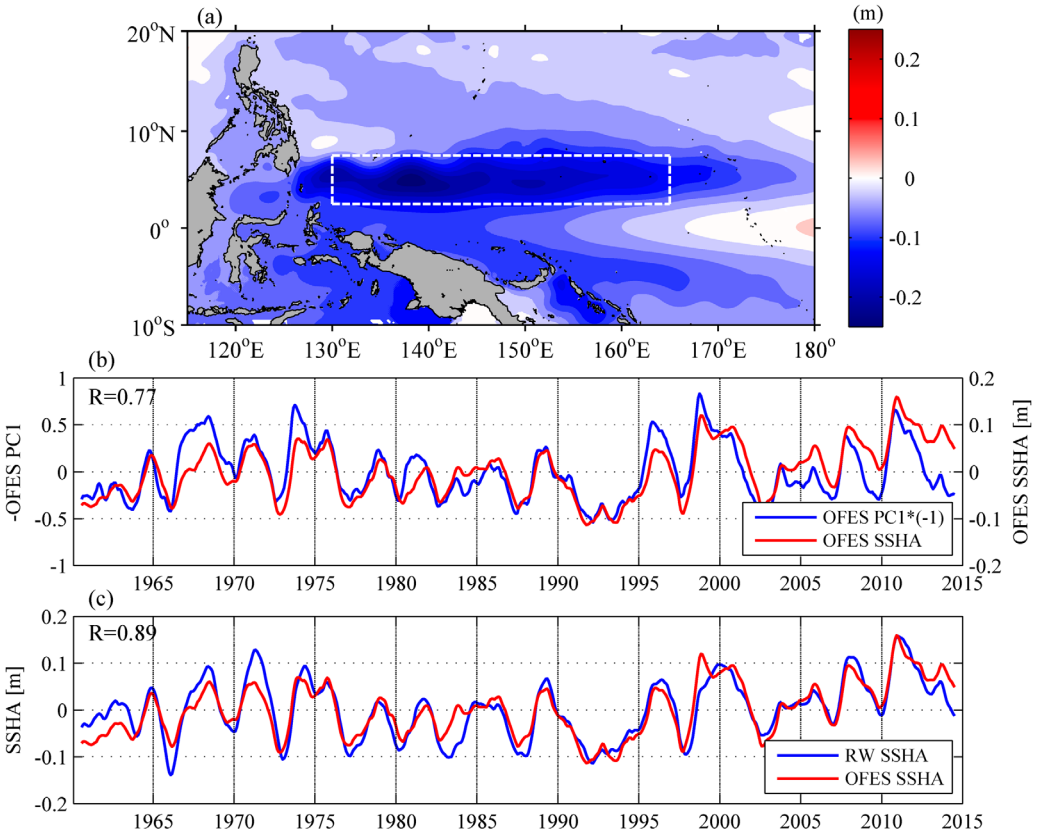


**Figure 9.** (a) Distribution of SSH anomalies regressed to PC1 shown in Figure 4b. (b) Time series of negative PC1 (blue line) versus the SSH anomalies averaged in the box of 2.5°N–7.5°N and 130°E–165°E (red line). Location of the box is indicated by the white dashed line in Figure 9a. (c) Time series of the SSH anomalies in the 2.5°N–7.5°N and 130°E–165°E box from the OFES simulation (red line) versus from the $1^1/_2$-layer reduced-gravity model (blue line). All SSH anomaly time series have been subjected to a 13 month running-mean filtering.

$$S(X) \equiv 1 - \frac{\langle [\overline{h'}(x_e,t) - \overline{h'}(X,t)]^2 \rangle}{\langle \overline{h'}^2(x_e,t) \rangle}, \tag{7}$$

where $\langle\rangle$ denotes the ensemble average in time. The plot reveals that the SSH variation in the NECC box is forced relatively uniformly by wind across the equatorial Pacific basin from 150°E to 120°W. This forcing pattern of the NECC variability is very different from that in the higher latitude band of the NEC (12°N–14°N), where wind forcing on the interannual SSH variability in the western Pacific is largely confined to the west of the dateline [*Qiu and Chen*, 2010, their Figure 9].

To confirm this subtle difference between the latitudinal bands further, we plot in Figure 10b the surface wind stress vector and curl field regressed to the EOF PC1. In connection with the development of El Niño, weakening of the trades along the equator generates a band of zonally coherent positive wind stress curl along 2°N–9°N and it is this zonal band of coherent forcing that causes the cumulative SSH drops in the western NECC region of our interest (recall Figure 9a). Physically, emergence of this anomalous positive wind stress curl band along 2°N–9°N corresponds to the strengthening and equatorward shift of the Intertropical Convergence Zone (ITCZ) during the El Niño events.

### 5.2. Interdecadal NECC Variability

The interdecadal NECC variability, as we noted in section 4.2, is characterized by its decreasing in zonal transport and its poleward migrating and broadening in axis over the 1960–2014 period (recall Figure 8). To gain a better understanding of these long-term changes, it is again beneficial to adopt the wind-forced $1^1/_2$-layer reduced-gravity model. Figure 11 compares the SSH field zonally averaged in the 135°E–155°E band as a function of latitude and time from (a) the $1^1/_2$-layer reduced-gravity model versus (b) the OFES simulation. In both (a) and (b), there appears a clear poleward migration in the SSH trough that existed near 7°N in

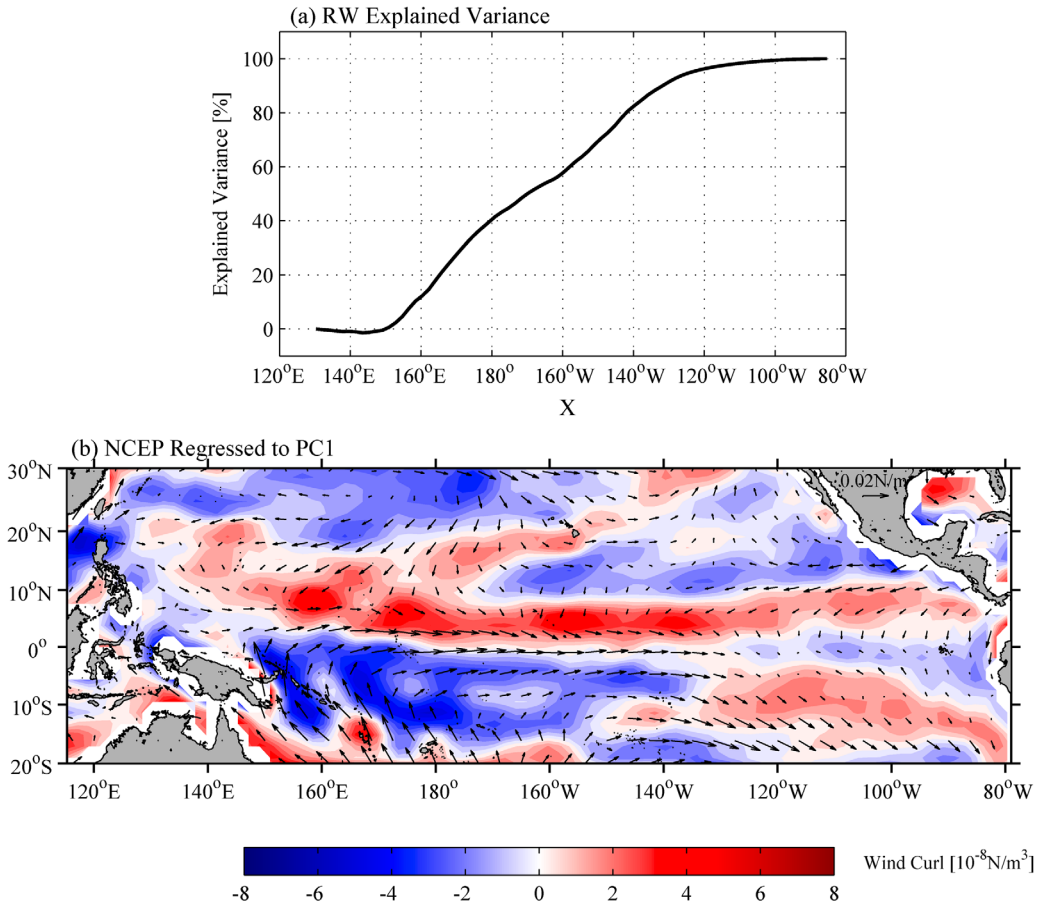


**Figure 10.** (a) Explained percent of variance of SSH anomalies in the box of 2.5°N–7.5°N and 130°E165°E by the cumulative wind forcing from 130°E to longitude *X*. See equations (6) and (7) and the text for details. (b) NCEP-NCAR wind stress vector and curl (in color) regressed to PC1 shown in Figure 4b.

the 1960s and shifted to near 9°N in the 2000s. Since this SSH trough corresponds to the northern edge of the NECC, its poleward migration is indicative of the movement of the NECC itself. To evaluate the NECC's migration quantitatively from the $1^1/_2$-layer reduced-gravity model, we plot in Figure 12b the time series of the center latitude between the SSH trough and the SSH ridge near 2°N shown in Figure 11a. Dynamically, the SSH ridge near 2°N signifies the southern edge of the NECC. Despite being derived from the simple dynamical model, the NECC axis variability shown in Figure 12b captures well the interdecadal axis migration modeled by the eddy-resolving OFES simulation (cf., Figure 8b). The linear correlation coefficient between the two time series is 0.57.

From Figure 11a, it is equally discernible that the difference between the SSH trough and the SSH ridge along 2°N, which corresponds to the upper ocean transport of the NECC, has decreased over the past 50 years. To quantify this decreasing trend, we plot in Figure 12a the SSH difference time series between 1.9°N and 7.6°N based on Figure 11a. Like the NECC axis variability described in the preceding paragraph, the $1^1/_2$-layer reduced-gravity model-inferred NECC transport variability also compares well with the eddy-resolving OFES simulation result. The linear correlation coefficient between Figures 12a and 8a reaches 0.67.

The success of the $1^1/_2$-layer reduced-gravity model in simulating the interdecadal NECC variations suggests that instead of the internal oceanic variability, the external wind forcing is the primary cause. In order to relate the long-term wind changes in the Pacific more explicitly to the NECC variability, we plot in Figure 13 the NCEP-NCAR wind stress curl field zonally averaged from the eastern boundary to 135°E (or the western boundary in the southern hemisphere) across the Pacific basin. With the NECC being the confluent outflow for the tropical wind-driven gyres, the most relevant wind forcing responsible for its variability falls in the negative curl band between the equator and 10°N. On the interdecadal timescales, Figure 13 reveals that this negative curl band

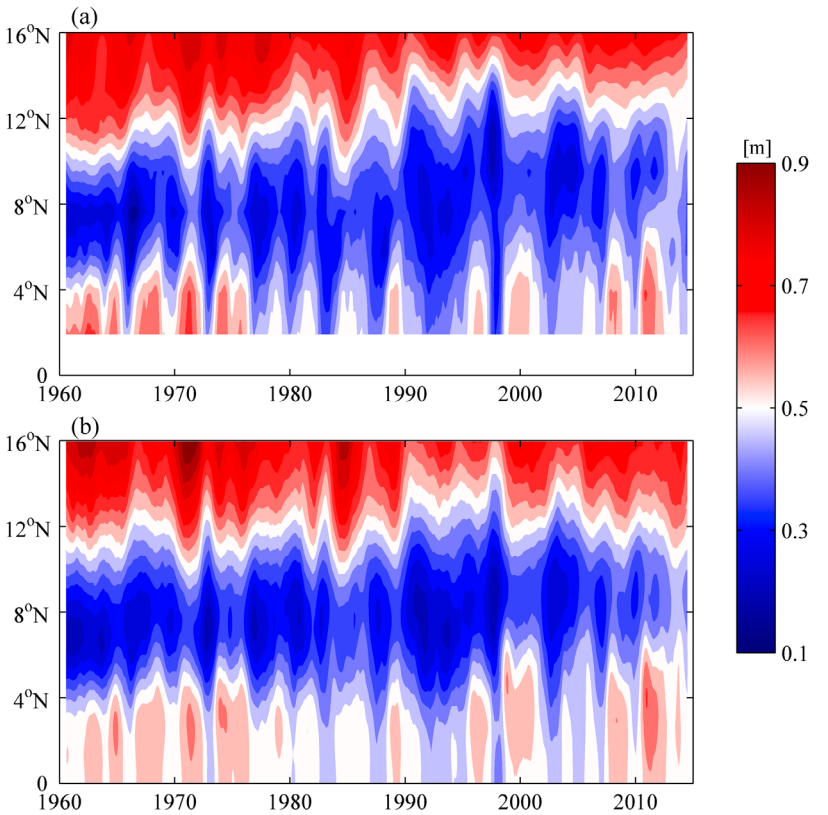


**Figure 11.** (a) SSH values averaged from 135°E and 155°E as a function of time and latitude from the $1^1/_2$-layer reduced-gravity model. The time-mean SSH value is taken from the OFES simulation and a 13 month running-mean filter has been applied. (b) Same as Figure 11a except from the OFES simulation.

expanded poleward, while decreasing in intensity over the period of 1960–2014. At the same time, there was a concurrent broadening in the negative curl region toward the equator. These long-term changes in the wind stress curl field are consistent with the three respective aspects of the interdecadal NECC variability shown in Figure 8. Specifically, the decrease in curl intensity caused the weakening of the NECC, the poleward shift of the overall negative curl band resulted in the corresponding shift in the NECC axis, and the broadening in the negative curl band both poleward and equatorward was responsible for the enhanced lateral excursions of the NECC axis.

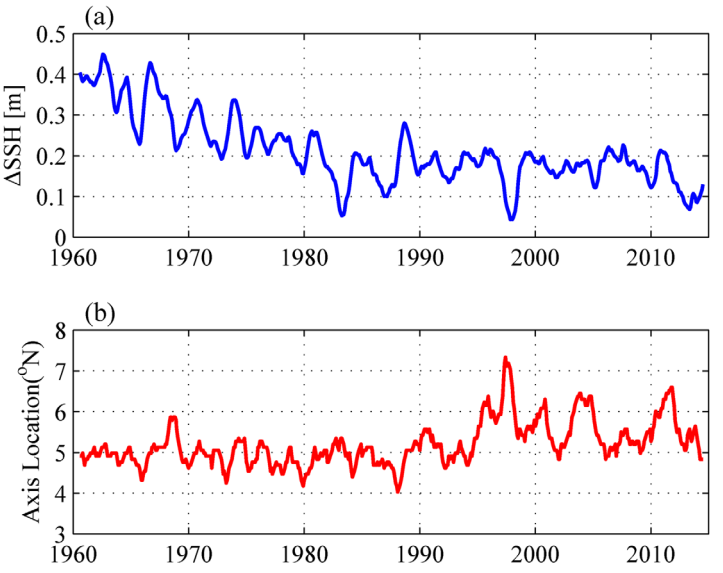


**Figure 12.** (a) Time series of SSH difference between 1.9°N and 7.6°N averaged zonally from 135°E to 155°E based on the $1^1/_2$-layer reduced-gravity model shown in Figure 11a. (b) Same as Figure 12a except for the NECC's axis location defined as the center latitude between the SSH trough near 8°N and the SSH ridge near 2°N.

## 6. Discussion and Conclusions

Interannual and longer timescale variations of the NECC in the tropical western Pacific are investigated in this study using the output of the eddy-resolving OFES simulation from 1960 to 2014. Forced by the

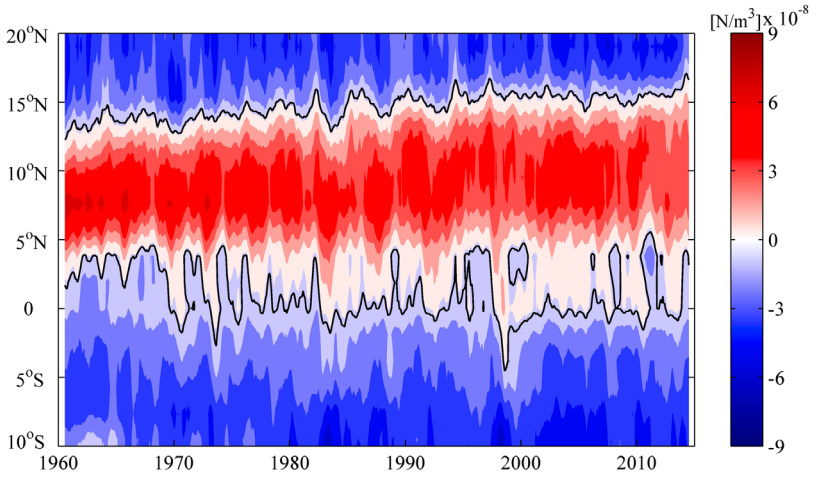


**Figure 13.** NCEP-NCAR wind-stress curl values zonally averaged from the Pacific Ocean eastern boundary to 135°E (or the western boundary in the southern hemisphere) as a function of time and latitude. A 13 month running-mean filter has been applied in time.

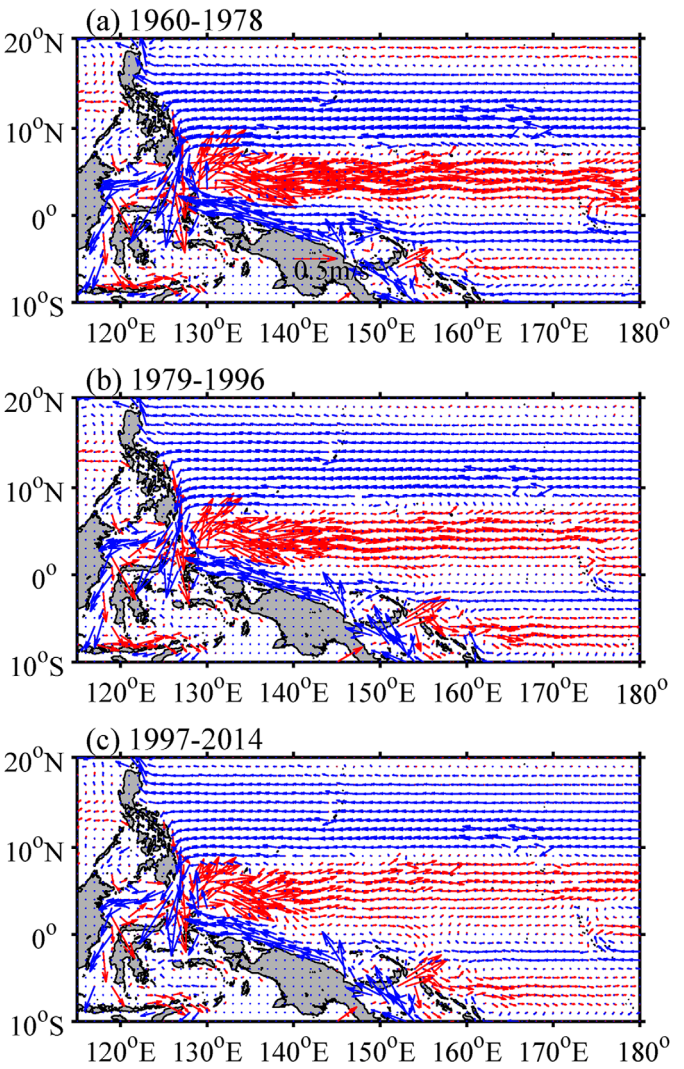


**Figure 14.** Mean upper ocean (0–150 m) velocity field averaged in (a) 1960–1978, (b) 1979–1996, and (c) 1997–2014 from the OFES simulation.

NCEP-NCAR reanalysis surface momentum and heat fluxes, the OFES-simulated sea level and NEC/NECC variations are found to compare favorably with the available tide gauge sea level measurements in the tropical western Pacific, as well as the JMA repeat hydrographic surveys along the 137°E meridian. The NECC variability is confined to the 150 m layer of the upper ocean and 56% of its variance can be explained by the first two EOF modes. The leading mode of the NECC variability is interannually varying and it constitutes an integral part of the tropical ENSO phenomenon. As an El Niño event develops, the NECC tends to intensify in strength and migrate equatorward. Averaged zonally from 135°E to 155°E, the NECC in the upper ocean (0–150 m) has a transport of 23.8 Sv (18.4 Sv) and an axis location at 3.7°N (5.2°N) during the El Niño (La Niña) years. The ENSO-related NECC variability shows a 1 month lead ahead of the Niño-3.4 index.

The second mode of the NECC variability reflects the changes on the interdecadal timescales.

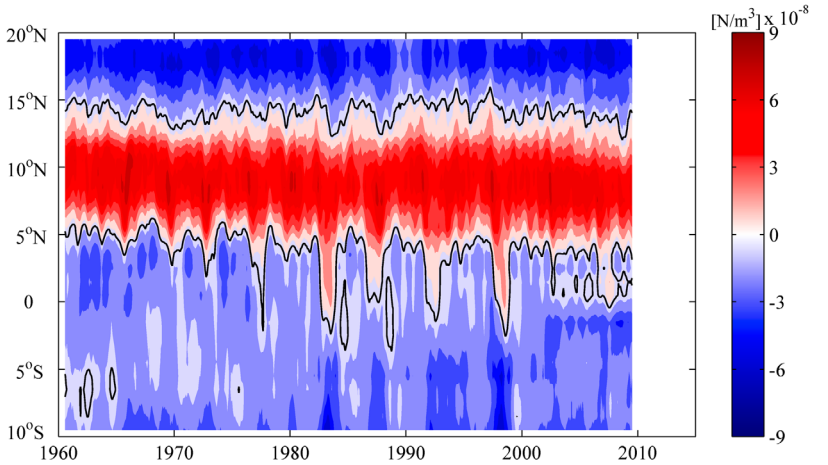


**Figure 15.** ECMWF ORA-S3 wind-stress curl values zonally averaged from the Pacific Ocean eastern boundary to 135°E (or the western boundary in the southern hemisphere) as a function of time and latitude. A 13 month running-mean filter has been applied in time.

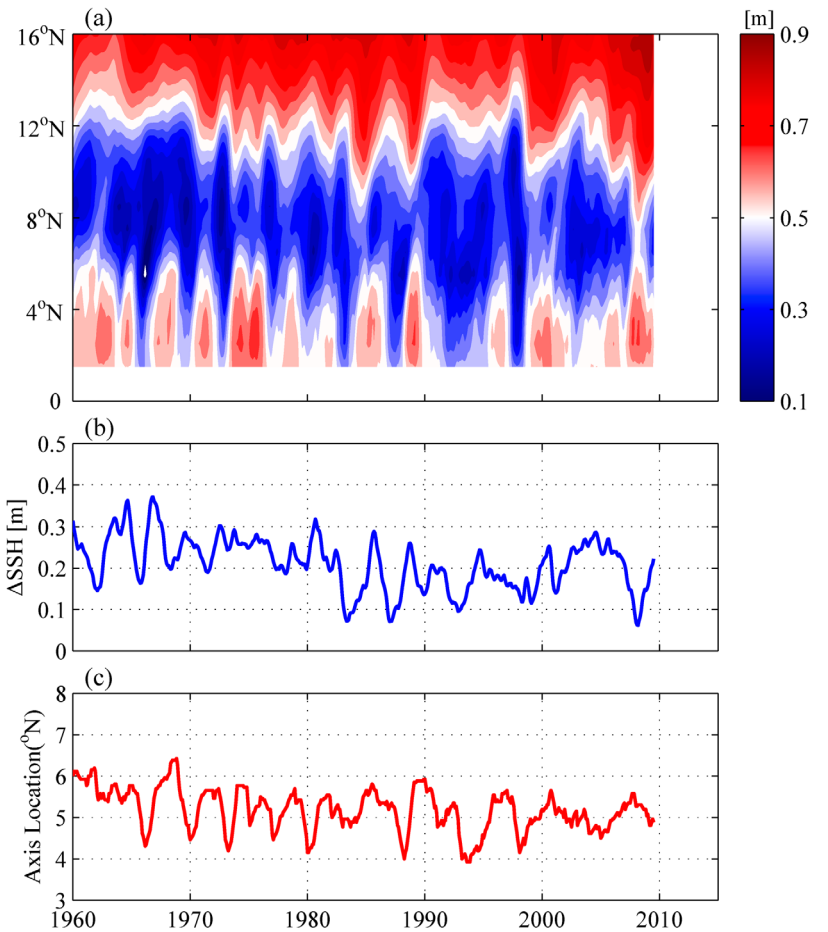


**Figure 16.** (a) SSH values averaged from 135°E and 155°E as a function of time and latitude from the 1½-layer reduced-gravity model using the ECMW ORA-S3 wind. The time-mean SSH value is taken from the OFES simulation and a 13 month running-mean filter has been applied. (b) Time series of SSH difference between 1.9°N and 7.6°N averaged zonally from 135°E to 155°E based on the 1½-layer reduced-gravity model shown in Figure 16a. (c) Same as Figure 16b except for the NECC's axis location defined as the center latitude between the SSH trough near 8°N and the SSH ridge near 2°N.

Over the period of 1960–2014 and averaged from 135°E to 155°E, the NECC was observed to have lessened in its zonal transport from 35 Sv to 25 Sv, its axis migrated poleward from 4°N to 5°N, and its axis width-scale widened from 100 to 130 km. Unlike the ENSO-related mode-1 variability, these interdecadal variations of the NECC have not been detected by existing NECC studies. To better visualize the interdecadal variations, we contrast in Figure 14 the time-mean upper ocean (0–150 m) velocity field in (a) 1960–1978, (b) 1979–1996, and (c) 1997–2014, respectively. The progressive weakening in the NECC strength, its axis shifting toward a higher latitude, and its widening in width are readily discernible in these composite maps.

Both of the NECC's interannual and interdecadal variability can be quantitatively evaluated using a $1^1/_2$-layer reduced-gravity model forced by the NCEP-NCAR reanalysis wind stress data. For the ENSO-related interannual signals, the NECC variability is found to be approximated well by the SSH anomalies in the 2.5°N–7.5°N, 130°E–165°E box. An examination into the wind forcing field reveals that rather than confined to the western Pacific, wind stress curl forcing accumulated across the enter Pacific basin along 2.5°N–7.5°N contributes to the variability of the NECC. For the interdecadal NECC variations, long-term changes in the negative wind stress curl field along the 0°N–10°N band are found to be the driving force. During the period of 1960–2014, the negative wind stress curl weakened and shifted poleward. These wind field changes generated the corresponding changes in the NECC's transport and axis location. At the same time, the equatorward expansion in the negative wind stress curl band induced the widening in the eastward-flowing NECC.

Since the global OFES simulation was forced by the NCEP-NCAR reanalysis wind stresses, we have explored the causes for the NECC variability using the $1^1/_2$-layer reduced-gravity model forced by the same wind stress product. Besides the NCEP-NCAR reanalysis product, another wind stress product that is commonly used to drive ocean general circulation models, is that of the European Center for Medium-Range Weather Forecasts (ECMWF) Ocean Analysis System ORA-S3 [*Balmaseda et al*., 2008]. While the time-varying wind stress signals reveal robust features on interannual timescales, those two reanalysis products can differ as the timescale becomes longer. For example, Figure 15 shows the wind stress curl field zonally averaged from the eastern boundary to 135°E (or the western boundary in the southern hemisphere) across the Pacific basin based on the ECMWF ORA-S3 wind stress data. Compared to the same field calculated from the NCEP-NCAR data shown in Figure 13, it reveals that while the positive wind stress curl band between the equator and 15°N in both products expanded in latitude over the past half century, the northward migration by the zero wind stress curl line near 15°N seen in Figure 13 is not detected in the ECMWF ORA-S3 result of Figure 15 [*Chen and Wu*, 2012].

This difference in the long-term changes of wind stress curl impacts the multidecadal wind-forced NECC variations. To quantify these variations, we conduct the same analyses as those described in section 5.2 with the NCEP-NCAR wind stress data replaced by that of ECMWF ORA-S3. Figure 16a shows the SSH field zonally averaged in the 135°E-155°E band as a function of latitude and time from the ORA-S3 forced $1^1/_2$-layer reduced-gravity model. From this model output and using the same methodology for deriving Figure 12, we plot in Figures 16b and 16c the time series of the SSH difference across the NECC and the axis position of the NECC, respectively. A comparison between Figures 12a and 16b indicates that the multidecadal variations in NECC's intensity are, by and large consistent between the NCEP-NCAR and ORA-S3 results; specifically, the NECC was stronger before 1980s than it is in the recent three decades. On the other hand, the long-term northward migration signal of the NECC seen in the NCEP-NCAR time series (Figure 12b) is not present in the ORA-S3 time series (Figure 16c). Due to lack of the long-term in situ measurements for the NECC, it is difficult at this stage to judge the differing representations between these two model results.

Throughout this study, we have focused on the dynamical changes of the NECC relating to its transport and axis position. As the NECC constitutes a sharp lateral boundary between the water masses originating from the North and South Pacific Oceans, its interannual and interdecadal changes can potentially affect the regional water mass properties inside the warm pool, as well as those carried eastward by the NECC toward the eastern tropical Pacific. It will be important for future studies to quantify the thermodynamical impact resulted from the interannual and interdecadal NECC changes.

**Acknowledgments**
We thank the two reviewers whose detailed comments helped improve the early version of the paper. The OFES simulation was conducted on the Earth Simulator under the support of JAMSTEC. The OFES-NCEP output used in our study is obtained from APDRC, University of Hawaii (http://apdrc.soest.hawaii.edu). This study is supported by the National Natural Science Foundation of China (grant 41521005 and 41525019), the Chinese Academy of Sciences (grant XDA11010000), the State Oceanic Administration of China (GASI-IPOVAI-02), the National Basic Research Program of China (grant 2014CB745001), the Natural Science Foundation of China (grant 41522601), the Open Project Program of State Key Laboratory of Tropical Oceanography (LTOZZ1501), the CAS/SAFEA International Partnership Program for Creative Research Teams, and the China Scholarship Council.

## References

Balmaseda, M. A., A. Vidard, and D. L. T. Anderson (2008), The ECMWF Ocean Analysis System: ORA-S3, *Mon. Weather Rev.*, *136*, 3018–3034.
Bonjean, F., and G. S. E. Lagerloef (2002), Diagnostic model and analysis of the surface currents in the tropical Pacific Ocean, *J. Phys. Oceanogr.*, *32*, 2938–2954.
Boyer, T. P., and S. Levitus (1997), *Objective Analyses of Temperature and Salinity for the World Ocean on a 1/4° Grid*, vol. 11, *NOAA Atlas NESDIS*, Natl. Oceanic and Atmos. Admin., Silver Spring, Md.
Capotondi, A., and M. A. Alexander (2001), Rossby waves in the tropical North Pacific and their role in decadal thermocline variability, *J. Phys. Oceanogr.*, *31*, 3496–3515.
Capotondi, A., M. A. Alexander, and C. Deser (2003), Why are there Rossby wave maxima in the Pacific at 10°S and 13°N?, *J. Phys. Oceanogr.*, *33*, 1549–1563.
Chen, X., B. Qiu, S. Chen, Y. Qi, and Y. Du (2015), Seasonal eddy kinetic energy modulations along the North Equatorial Countercurrent in the western Pacific, *J. Geophys. Res. Oceans*, *120*, 6351–6362, doi:10.1002/2015JC011054.
Chen, Z., and L. Wu (2012), Long-term change of the Pacific North Equatorial Current bifurcation in SODA, *J. Geophys. Res.*, *117*, C06016, doi:10.1029/2011JC007814.
Clement, A. C., R. Seager, and R. Murtugudde (2005), Why are the tropical warm pool?, *J. Clim.*, *18*, 5294–5311, doi:10.1175/JCLI3582.1.
Delcroix, T., G. Eldin, and G. Eldin (1987), Upper ocean water masses and transports in the western tropical Pacific (165°E), *J. Phys. Oceanogr.*, *17*, 2248–2262, doi:10.1175/1520-0485(1987)017<2248:UOWMAT>2.0.CO;2.
Donguy, J.-R., and G. Meyers (1996), Mean annual variation of transports of major currents in the tropical Pacific Ocean, *Deep Sea Res., Part I*, *43*(7), 1105–1122, doi:10.1016/0967-0637(96)00047-7.
Fu, L.-L., and B. Qiu (2002), Low-frequency variability of the North Pacific Ocean: The roles of boundary-driven and wind-driven baroclinic Rossby waves, *J. Geophys. Res.*, *107*(C12), 3220, doi:10.1029/2001JC001131.
Gordon, A. L., and R. A. Fine (1996), Pathways of water between the Pacific and Indian oceans in the Indonesian seas, *Nature*, *379*(6561), 146–149.
Gouriou, Y., and J. Toole (1993), Mean circulation of the upper layers of the western equatorial Pacific Ocean, *J. Geophys. Res.*, *98*, 22,495–22,520.
Heron, S. F., E. J. Metzger, and W. J. Skirving (2006), Seasonal variations of the ocean surface circulation in the vicinity of Palau, *J. Oceanogr.*, *62*(4), 413–426, doi:10.1007/s10872-006-0065-3.
Hsin, Y.-C., and B. Qiu (2012a), Seasonal fluctuations of the surface North Equatorial Countercurrent (NECC) across the Pacific basin, *J. Geophys. Res.*, *117*, C06001, doi:10.1029/2011JC007794.
Hsin, Y.-C., and B. Qiu (2012b), The impact of Eastern-Pacific versus Central-Pacific El Niño on the North Equatorial Countercurrent in the Pacific Ocean, *J. Geophys. Res.*, *117*, C11017, doi:10.1029/2012JC008362.
Hu, D., et al. (2015), Pacific western boundary currents and their roles in climate, *Nature*, *522*, 299–308.
Johnson, G. C., B. M. Sloyan, W. S. Kessler, and K. E. McTaggart (2002), Direct measurements of upper ocean currents and water properties across the tropical Pacific during the 1990s, *Prog. Oceanogr.*, *52*(1), 31–61, doi:10.1016/S0079-6611(02)00021-6.
Kalnay, E., et al. (1996), The NCEP/NCAR 40-year reanalysis project, *Bull. Am. Meteorol. Soc.*, *77*, 437–471, doi:10.1175/1520-0477077<0437:TNYR>2.0.CO;2.
Kashino, Y., E. Firing, P. Hacker, A. Sulaiman, and Lukiyanto (2001), Currents in the Celebes and Maluku Seas, February 1999, *Geophys. Res. Lett.*, *28*, 1263–1266.
Kessler, W. S. (1990), Observation of long Rossby waves in the northern tropical Pacific, *J. Geophys. Res.*, *95*, 5183–5217.
Lukas, R., E. Firing, P. Hacker, P. L. Richardson, C. A. Collins, R. Fine, and R. Gammon (1991), Observations of the Mindanao Current during the Western Equatorial Pacific Ocean Circulation Study, *J. Geophys. Res.*, *96*, 7089–7104.
Masumoto, Y., et al. (2004), A fifty-year eddy-resolving simulation of the world ocean: Preliminary outcomes of OFES (OGCM for the Earth Simulator), *J. Earth Simulator*, *1*, 35–56.
Meyers, G. (1979), On the annual Rossby wave in the tropical North Pacific Ocean, *J. Phys. Oceanogr.*, *9*(4), 663–674, doi:10.1175/1520-0485(1979)009<0663:OTARWI>2.0.CO;2.
Meyers, G., and J. R. Donguy (1984), The North Equatorial Counter Current and heat storage in the western Pacific Ocean during 1982–83, *Nature*, *312*, 258–260.
Nakano, T., I. Kaneko, M. Endoh, and M. Kamachi (2005), Interannual and decadal variabilities of NPIW salinity minimum core observed along JMA's hydrographic repeat sections, *J. Oceanogr.*, *61*, 681–697, doi:10.1007/s10872-005-0076-5.
Pacanowski, R. C., and S. M. Griffies (2000), *MOM 3.0 Manual, Technical Report 4*, 680 pp., Geophys. Fluid Dyn. Lab., Princeton, N. J.
Philander, S. G. H. (1990), *El Niño, La Niña, and the Southern Oscillation*, pp. 293, Academic Press, San Diego, Calif.
Picaut, J., and T. Delcroix (1995), Equatorial wave sequence associated with warm pool displacement during the 1986-1989 El Niño-La Niña, *J. Geophys. Res.*, *100*, 18,393–18,408.
Qiu, B., and T. M. Joyce (1992), Interannual variability in the mid- and low-latitude western North Pacific, *J. Phys. Oceanogr.*, *22*, 1062–1079, doi:10.1175/1520-0485(1992)022<1062:IVITMA>2.0.CO;2.
Qiu, B., and R. Lukas (1996), Seasonal and interannual variability of the North Equatorial Current, the Mindanao Current and the Kuroshio along the Pacific western boundary, *J. Geophys. Res.*, *101*, 12,315–12,330.
Qiu, B., and S. Chen (2010), Interannual-to-decadal variability in the bifurcation of the North Equatorial Current off the Philippines, *J. Phys. Oceanogr.*, *40*, 2525–2538.
Qiu, B., D. L. Rudnick, I. Cerovecki, B. D. Cornuelle, S. Chen, M. C. Schonau, J. L. McClean, and G. Gopalakrishnan (2015), The Pacific North Equatorial Current: New insights from the Origins of the Kuroshio and Mindanao Currents (OKMC) project, *Oceanography*, *28*(4), 24–33.
Reverdin, G., C. Frankignoul, E. Kestenare, and M. J. Mcphaden (1994), Seasonal variability in the surface currents of the equatorial Pacific, *J. Geophys. Res.*, *99*, 20,323–20,344.
Sasaki, H., M. Nonaka, Y. Masumoto, Y. Sasai, H. Uehara, and H. Sakuma (2008), An eddy-resolving hindcast simulation of the quasiglobal ocean from 1950 to 2003 on the Earth Simulator, in *High Resolution Numerical Modeling of the Atmosphere and Ocean*, edited by K. Hamilton and W. Ohfuchi, pp. 157–185, Springer, N. Y.
Tozuka, T., T. Kagimoto, Y. Masumoto, and T. Yamagata (2002), Simulated multiscale variations in the western tropical Pacific: The Mindanao Dome revisited, *J. Phys. Oceanogr.*, *32*, 1338–1358, doi:10.1175/1520-0485(2002)032<1338:SMVITW>2.0.CO;2.
Zhao, J., Y. Li, and F. Wang (2013), Dynamical responses of the west Pacific North Equatorial Countercurrent (NECC) system to El Niño events, *J. Geophys. Res. Oceans*, *118*, 2828–2844, doi:10.1002/jgrc.20196.